

# **Dynamic Model Integration and Simulation Engine- (DMISE-) assisted design of future sensor networks in support of Space Traffic Management**

**Douglas A. Hope, Megan Birch, Christopher E. Cordell, Jr., Keith F. Prussing, and Christopher R. Valenta**

*Georgia Tech Research Institute, Atlanta GA*

## **ABSTRACT**

As the number of satellites and space debris increases, we begin to face the ever more likely scenario of space objects colliding. The resulting collisions could create a debris field, cascading into additional collisions and initiating a chain reaction. Due to the uncontrolled and unknown amount of debris, the resulting Kessler effect could render large parts of the orbital regime unusable for space operations and navigation. Preventing this Kessler effect is a significant motivation for developing Space Traffic Management (STM). The major thrust of STM focuses on identifying space debris, performing conjunction analysis, and subsequently mitigating by maneuvering of active satellites. The proliferation of mega-satellite constellations, such as Starlink (SpaceX), Kuiper Systems (Amazon), and Doves (Planet Labs) in Low-Earth-Orbit (LEO), will create challenges in performing STM. Given this expected increase in the number of resident space objects (RSOs), managing space traffic will require more advanced technology and resources to provide accurate and timely conjunction analysis and knowledge about the presence and distribution of debris and other space objects in the orbital regimes occupied by mega satellite constellations. This paper presents a suite of modeling and simulation (M&S) tools that integrate models for space object geometry, motion, environmental effects, and camera observations of scenes as a tool for STM analysis, target identification, and classification. Specifically, this manuscript presents preliminary results from verification of the M&S tool for both ground- and space-based optical and infrared imaging scenarios. Example models of particular engagement scenarios, such as all-sky surveys of RSOs and a space-based imager scanning orbital belts for debris, show realistic imagery for different observing conditions and varying sensor parameters. Ultimately, we envision our M&S tools supporting the design and development of future ground- and space-based sensors to support the goals of STM.

## **1. INTRODUCTION**

The long-term monitoring of satellites and debris in the space environment represents a crucial component of Space Domain Awareness (SDA) and subsequent Space Traffic Management (STM). Both SDA and STM depend on the long-term monitoring of satellites and space debris, a task, for the most part, is accomplished by ground-based sensors. While ground-based sensors offer distinct advantages, such as high resolution and large apertures for faint imaging of targets, many scenarios exist where numerous space-based sensors could provide information not obtainable from Earth. Thus, any successful future STM will rely on both ground- and space-based sensors and how they might collaboratively address specific needs of STM.

Characterizing space objects requires measuring the emitted and reflected electromagnetic radiation from space objects. Both radio and optical frequencies provide essential and complementary information RSOs. Radio frequencies such as RADAR play a crucial role in detecting, computing orbital trajectories, and obtaining size estimates of RSOs. In contrast, optical and infrared frequencies yield essential information on object RSO morphology and surface materials. Our efforts in this paper primarily address the role of visual and infrared sensors in supporting STM goals. We demonstrate the integral part of M&S in designing and optimizing future ground- and space-based sensors and how it offers a new platform for studying the simultaneous interactions of numerous space objects to support efforts of STM to mitigate collisions. Electro-optical (EO) sensors address a wide range of problems in SDA, ranging from satellite custody, photometric change detection, surface material characterization,

and spatial characterization. Fig 1 shows a summary of the variety of different research and contributing EO-sensors for SDA.

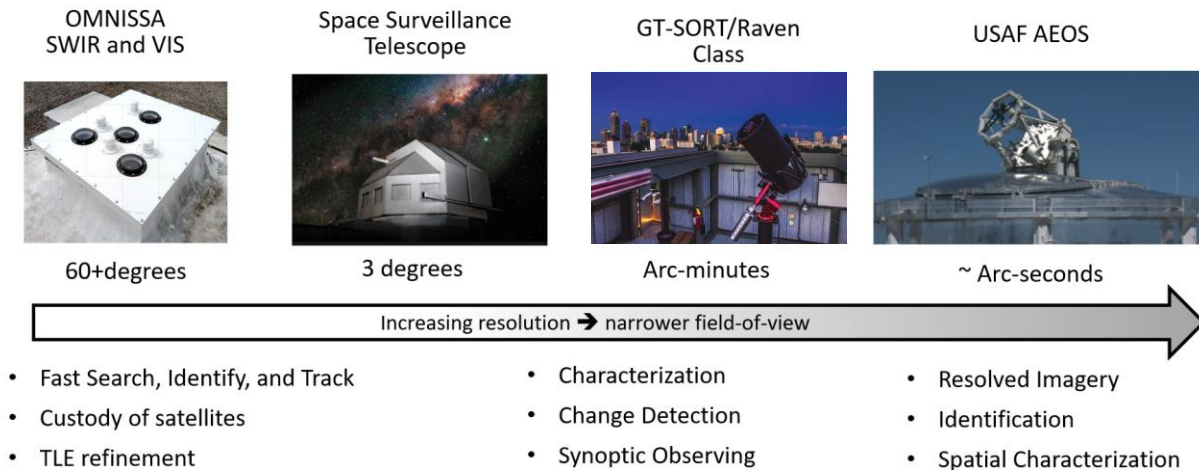


Fig 1: A variety of EO sensors address specific tasks related to SDA.

Wide field-of-view (FOV) imagers can see up to 90-degree views of the sky and thus address the problems of rapidly finding and identifying objects based on their movement across the sky relative to the background stars. The Omnidirectional Space Situational Awareness (OMNISSA) camera, initially designed in [1], is a wide-field imager that operates at visible wavelengths and can image a 90-degree area of the sky. More recently, upgrades to this instrument also support a short-wave infrared (SWIR) imaging capability. Other large imagers, such as the Space Surveillance Telescope, use a 1-3 degree field-of-view to search and track faint objects in the geostationary belt [2]. Narrower FOV telescopes, such as the Georgia Tech Space Object Research Telescope (GT-SORT) [3] and the United States Air Force (USAF) Raven class [4] telescopes focus on characterizing resident space objects (RSOs) based on changes in their photometric signature. High-resolution telescopes such as the USAF AEOS 3.6m [5] and Starfire Optical Range 3.5m [6] telescopes have several arc-second FOVs and provide spatially resolved imagery of satellites in Low-Earth-Orbit (LEO).

The sensors shown in Fig. 1 represent the variety of optical and infrared imaging sensors and their role in supporting SDA. Each sensor addresses specific tasks that support SDA. Successfully integrating these different sensors to work collaboratively to achieve a high level of SDA and support of STM will rely on realistic models of these sensors and their observations of potentially interacting objects in the space environment.

## 2. MODELING THE SPACE ENVIRONMENT

To support studies for SDA, Georgia Tech Research Institute (GTRI) is leading an effort to build a comprehensive modeling and simulation (M&S) capability to address different engagement scenarios for space objects, such as one-on-one and many-on-many interactions. Algorithm development related to SDA will require analysis from M&S environments in addition to observations with actual telescopes and cameras, as observational opportunities can be limited and different sensor configurations may prove better at certain aspects of the problem. This strategy looks to a future where modeling and analyzing the interaction of multiple satellites as observed by an array of space- and ground-based sensors will be a requirement for developing SDA strategies.

The primary M&S toolset developed by GTRI includes two software components, the Dynamic Model Integration and Simulation Engine (DMISE) and the General High-Fidelity Omni-Spectral Toolbox (GHOST). DMISE provides the underlying definitions for scenario components and the architecture for a simulation of these components interacting with each other. GHOST provides specific models, component definitions, and other aspects related to band-accurate rendering of dynamic scenarios, of which the SDA problem is a prime consideration. The two primary components of DMISE are a core and utility library. The core library defines the general interfaces that make up a

simulation, including both the components (*Actors*) that will interact with each other and the observations (*Evaluators*) that will describe the state of a simulation at a given point in time. The utility library contains a collection of generically useful tools such as mathematical operations, motion model interfaces, and coordinate transformations. Fig 2 shows an overview of the DMISE architecture. On the left is the core library which shows the general simulation broken into two major subcomponents; the Simulation Unit which encompasses the *Actors* and their *Geometries* and the Evaluation Unit which encompasses the *Evaluators* that can query the state of the Simulation Unit. The querying of the simulation is done through the State interfaces. Above both of these subcomponents is the *Simulation Controller* which handles the initialization and advancement of time.

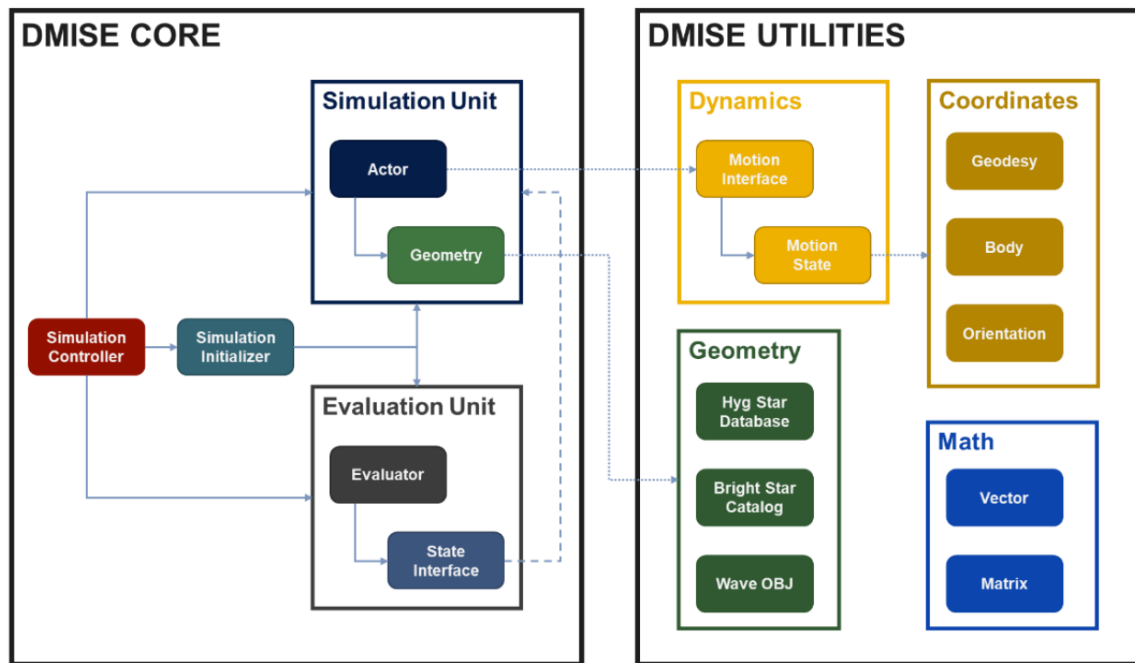


Fig 2: DMISE simulation architecture and supporting utilities.

On the other hand, the GHOST library comprises a suite of specific models for capturing the behavioral characteristics of particular components within a scenario. Fig 3 shows the current GHOST models, color-coordinated with the DMISE interfaces shown in Fig 2. The *Actors* include objects such as the star background, the sky, and a platform to represent physical bodies moving through the scenario. A more detailed description of each actor type within the simulation is provided in Table 1 **Error! Reference source not found.** For the *Evaluators*, we have implemented an OpenGL based rendering system that can be coupled with time-delay integration and an image output routine. This functionality provides a snapshot of the scene as seen by a camera. We have also implemented a method to output the location of the *Actors*' positions for post-processing and cross-referencing. Additionally, we implemented motion models relevant to the SDA problem such as constant position, SGP4, and two body orbit. A GHOST simulation is initialized at run-time based on a user-provided input file which describes the models by which each component should be defined.

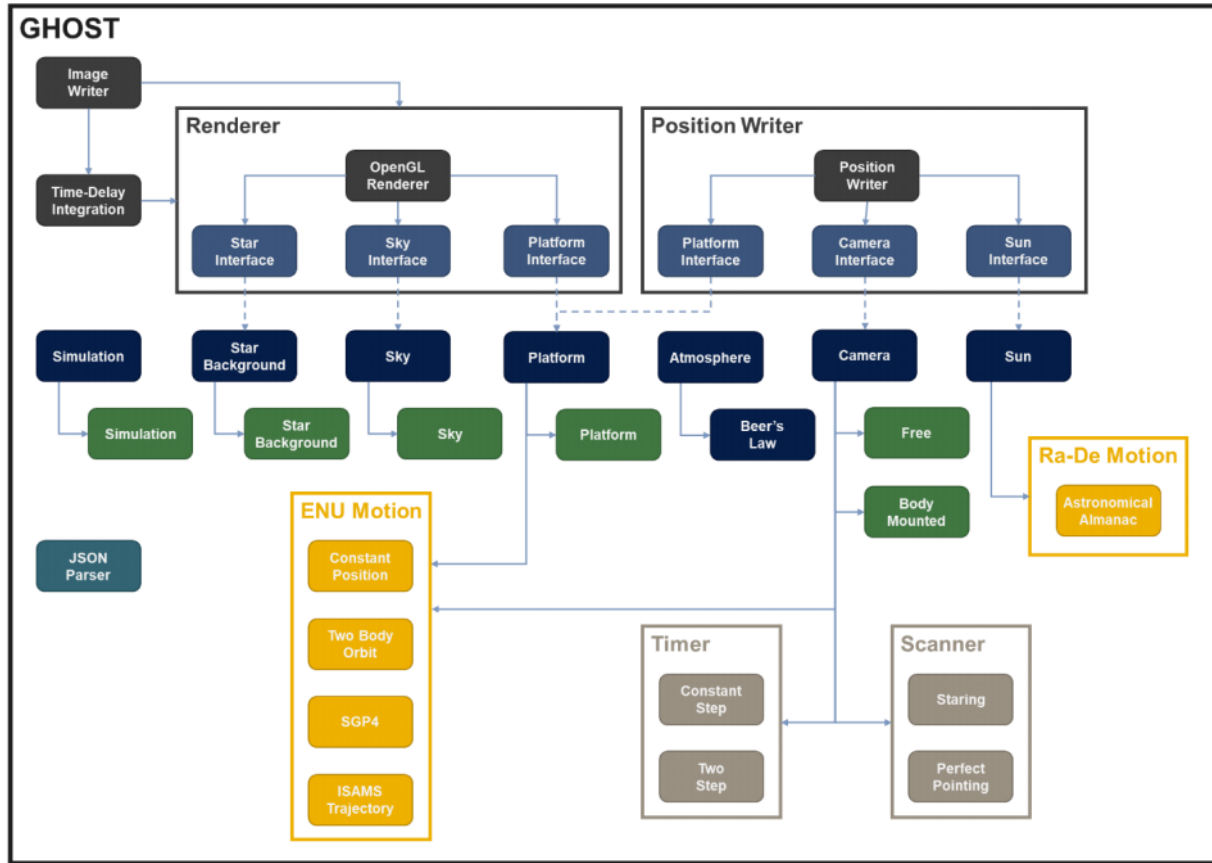


Fig 3: Current GHOST models color-coordinated with their respective DMISE interfaces.

Table 1: Overview of GHOST Actors.

Actor	Description
<b>Simulation</b>	Specifies the initial timing of the simulation, the reference ellipsoid for defining the 3-dimensional Earth, and the origin of the simulation for referencing ENU coordinates
<b>Star Background</b>	Specifies the position of the stars based on proper motion from the input file reference epoch date. Star positions are stored in the geometry using a celestial background with Right Ascension and Declination points for each star
<b>Sky</b>	Specifies the non-uniform sky background for dawn-to-dusk observations
<b>Platform</b>	Specifies a object or vehicle with a physical shape that can move within the scene. A Platform is used to represent an RSO, and the associated geometry stores facets, vertices, and materials for rendering the object
<b>Atmosphere</b>	Specifies the interface for general atmospheric perturbations that will affect the rendering of the scene
<b>Beer's Law</b>	Specifies a specific atmospheric model that implements Beer's Law for transmission of the light from objects to the observe
<b>Camera</b>	Specifies a model that represents the viewing geometry of a camera upon the scene. Cameras can either have a free geometry, where the camera moves independently within the simulation, or a body mounted geometry, where the camera is attached to a platform and moves with it
<b>Sun</b>	Specifies the model for capturing the position of the Sun for a given time of day

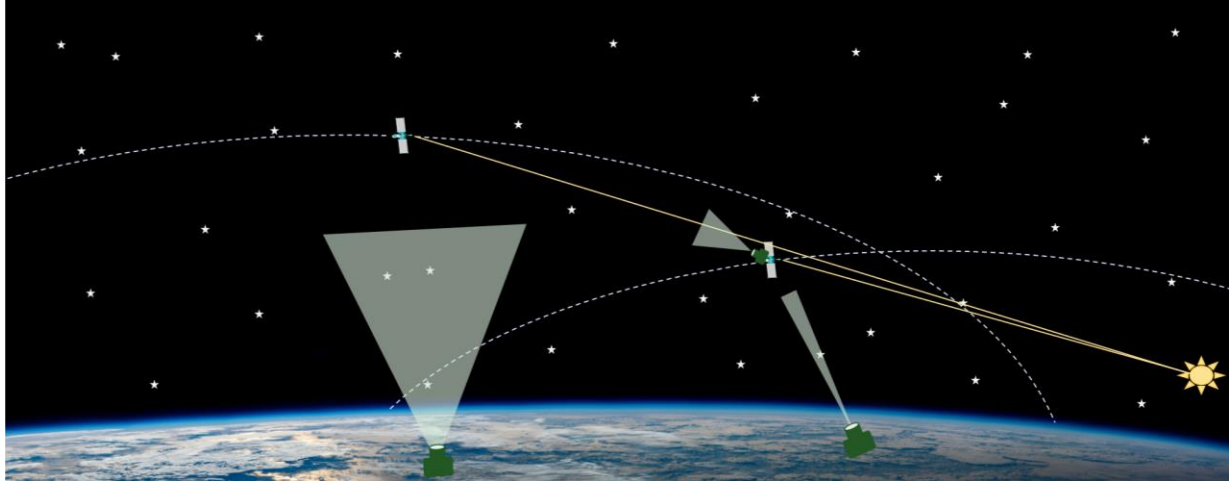


Fig 4: The simulated environment within GHOST.

Fig 4 shows a concrete example of the types of scenarios GHOST uses to analyze SDA scenarios. The primary components of interest are stars to serve as the background and reference points for astrometry, the Sun for providing light that reflects off satellites, satellite models on relevant orbits, cameras for observing the scene, terrestrial concerns for locating ground-based observations, providing reference frames and origin for positioning satellites within the simulation, and atmospheric effects. Next, we will discuss how each component maps into the GHOST framework.

A platform representing a satellite captures the geometry, the physical properties, and allows for specification of a motion model. While this motion could be a pre-generated trajectory loaded from a file, of particular relevance to an SDA scenario is the support within GHOST for the Simplified General Perturbations (SGP4) propagator. The SGP4 algorithm and library [7, 8] has been wrapped such that the actual SGP4 software is integrated into GHOST through a translation layer that converts the output of the SGP4 propagation into the required coordinate frame within the GHOST simulation. The physical geometry of the platform is defined as a set of facets and vertices, which can be read from any number of file types that provide such information. The Wave OBJ format has been used for this study [9].

The background environment for an SDA scenario is primarily driven by the stars on the celestial sphere and the Sun within the sky. The star geometry controls the location of the stars loaded within the simulation by specifying their right-ascension and declination based on the time since a specified epoch and their proper motion. Both the Hyg [10] and Yale Bright Star Catalog BSC [11] are supported. For the position of the Sun, the Astronomical Almanac [12] model of solar position within a right-ascension and declination reference frame is used.

A camera within the GHOST simulation provides models for positioning an observer within the scenario. A camera geometry is defined by its field-of-view and pixel counts as well as the eye location, look direction, and up direction of the observation. Within GHOST, a camera can be either a free camera that controls its own motion or a body-mounted camera that moves alongside the platform to which it is attached. GHOST provides interfaces for altering the direction of the camera look vector through scanning, although for this analysis the camera is assumed to stare along its boresight. Note that sensor-specific parameters, such as noise and diffraction limits, are accounted for later in the simulation.

At each point in time during a simulation at which a camera should take an image, GHOST uses OpenGL to render the scene from the viewpoint of that camera. The OpenGL evaluator consists of rendering interfaces for the stars, sky, and platforms. Stars are rendered as points with radiometrically accurate radiances based on their color temperature and the black body curve [13]. Platforms are rendered based on their source radiant intensity, which is effectively zero for a platform in space, and the reflection of solar illumination off of their geometry. The reflection takes into account obscuration from the Earth, where if the Earth reference ellipsoid is between the Sun and the platform, then there is no light to reflect. This image synthesis procedure provides realistic camera radiance images based on the amount of solar illumination and the materials specified for the satellite. Rendered images can be provided as static snapshots, effectively modeling an infinitesimally small exposure time, or as time-integrated imagery where many

static snapshots are integrated together to simulate the exposure time of a camera. Typically, wide-field imagers rely on the position of stars for angle only calculations to determine and update an orbital trajectory. However in some cases, the presence of stars can act as clutter in the background that can corrupt observations of the primary target of interest.

In addition to the primary output of rendered images, GHOST supports evaluators that can serve as output devices for the position of components within the simulation. Positions of cameras, platforms, and the Sun can be output at each time step, providing metadata to assist in analysis of the imagery and verification of the M&S results. In particular, the coordinate frame conversions are critical for this effort, as proper geolocation of the observation telescopes and the RSOs being observed must be maintained. The positioning of the objects in space is handled by the coordinate conversion methods implemented in the DMISE utility library along with the simulation start time and reference geodetic details stored in the Simulation, and the time evolution is handled by the simulation controller. Having the time and position handled by consistent utilities ensures each Actor in the scenario is in a consistent reference frame.

### 3. REALISTIC SENSOR MODELING

The GHOST M&S environment generates radiance maps of the scene as observed by each sensor in the simulation at different time steps. The second component of our effort includes development of optical and sensor modules that model the image formation and detection processes.

Blurring of images results from both diffraction and turbulence in the atmosphere. Both effects are modeled using a Fourier Optics model [14]. Blur due to diffraction depends on the aperture diameter  $D$  and the observing wavelength,  $\lambda$ . The optical diffraction-limited blur is modeled in the Fourier domain as a spatial filter function,

$$H_{DL}(\mathbf{u}) = \frac{2}{\pi} \left( \arccos(A(\mathbf{u})) - A(\mathbf{u})\sqrt{1 - A(\mathbf{u})^2} \right). \quad (1)$$

Here  $A(\mathbf{u}) = \frac{\lambda}{D} \sqrt{u_x^2 + u_y^2}$  measures the radial distance (scaled by the ratio of the observation wavelength  $\lambda$  and the aperture diameter  $D$ ) from the zero-frequency in the Fourier plane. The vector  $\mathbf{u}$  denotes a vector in the spatial frequency coordinates. The spatial frequency component  $u_x = \pi n_x / N_x$  where  $n_x$  is the  $n^{\text{th}}$  spatial frequency component, and  $N_x$  is the total number of samples along a linear dimension of the image.

Turbulence in the atmosphere limits the spatial resolution of ground-based telescopes thus further blurring imagery. The origins of the turbulence induced blur result from the diurnal heating and cooling of the atmosphere causing random fluctuations in the indices of refraction for air. These fluctuations, which vary spatially and temporally, are described by the structure function  $C_n^2(z)$ . The effect of turbulence is described by integrating a path weighted integral of the  $C_n^2(z)$  profile. The Fried [15,16] coherence diameter  $r_0$  describes the size of the seeing disk and is defined by

$$r_0 = [0.423k^2 \sec \zeta \int C_n^2(z) dz ]^{-3/5}, \quad (2)$$

where  $\zeta$  is the angle from zenith,  $k = \lambda/2\pi$ , and  $z$  is the altitude. The Fried parameter  $r_0$  describes the distance between two points in the wavefront where the RMS wavefront error caused by the turbulence is equal to 1 radian. Likewise, the coherence time  $\tau_0$  of the atmosphere depends on the wind speed  $|v|$  at an observation site and the  $r_0$  value,

$$\tau_0 = \frac{r_0}{|v|}. \quad (3)$$

Images with exposure times shorter or equal to the coherence time are *short exposure* images, and capture high spatial frequency information about a target. When the image exposure time exceeds the coherence time,  $t_{exp} \gg \tau_0$ , the images are *long exposure images*. This type of blurring is described by the long exposure optical transfer function [14]

$$H_{lexp}(\mathbf{u}) = \exp \left[ -3.44 \left( \frac{\lambda f |\mathbf{u}|}{r_0} \right)^{5/3} \right]. \quad (4)$$

Where  $\mathbf{u}$  denotes a spatial frequency, and  $f$  denotes the effective focal length of the telescope. The blur in the short exposure image is modeled using a Fourier optical model. The turbulence through which the light from the object propagates follows a Kolmogorov spectrum [17]. When imaging near zenith  $\zeta \sim 1$ , the turbulence causes primarily phase distortions and less amplitude distortions. The monochromatic incoherent point-spread function (PSF) can be expressed as the modulus-squared of the inverse Fourier Transform (IFT)  $\mathcal{F}^{-1}$  of the complex wavefront

$$h_{sexp}(\mathbf{x}) = |\mathcal{F}^{-1}\{A(\boldsymbol{\rho})e^{-i\phi(\boldsymbol{\rho})}\}|^2, \quad (5)$$

where  $\phi(\boldsymbol{\rho})$  is the turbulence induced wavefront phase,  $A(\boldsymbol{\rho})$  is the wavefront amplitude (unity),  $\boldsymbol{\rho}$  denotes a vector in the aperture plane, and  $\mathbf{x}$  denotes a vector in the image plane. The optical transfer function for a short exposure image is

$$H_{sexp}(\mathbf{u}) = \mathcal{F}\{h_{sexp}(\mathbf{x})\}, \quad (6)$$

where  $\mathcal{F}$  denotes the Fourier Transform operator. The primary effect of image detection is a spatial averaging of the irradiance distribution formed at the image plane. A square pixel cell in a focal plane array (FPA) of size  $w \times w$  performs a spatial average of the irradiance incident on the cell [18]. The Fourier representation of the 2D detector transfer function for the detector cell is

$$H_{samp}(\mathbf{u}) = \frac{\sin(wu_x)}{u_x} \frac{\sin(wu_y)}{u_y} \quad (6)$$

The sensor model converts the band integrated DMISE radiance scenes,  $R(\mathbf{x})$ , to an irradiance scene,  $f(\mathbf{x})$ , at the focal plane defined as

$$f(\mathbf{x}) = \frac{\pi}{4f_{\#}^2} R(\mathbf{x}). \quad (7)$$

Where  $f_{\#}^2$  is the ratio of the focal length and aperture diameter. The Fourier transform of the irradiance distribution yields its spectral representation

$$F(\mathbf{u}) = \mathcal{F}\{f(\mathbf{x})\}. \quad (8)$$

The Fourier representation of an image  $G(\mathbf{u})$  with optical and detection blur is computed as the product of the irradiance Fourier spectrum, and the transfer functions for optical diffraction, turbulence blur and spatial averaging by the detector, Eqs. (1), (4) and (6),

$$G(\mathbf{u}) = F(\mathbf{u})H_{DL}(\mathbf{u})H_{lexp}(\mathbf{u})H_{samp}(\mathbf{u}). \quad (9)$$

The inverse Fourier Transform yields the blurred image scene,

$$g(\mathbf{x}) = \mathcal{F}^{-1}\{G(\mathbf{u})\} \quad (10)$$

The amount of blur in the image  $g(\mathbf{x})$  depends on the observation wavelength. Thus, we model the image formation and detection over a limited spectral bandwidth corresponding to the observation filter bandwidth. The value for  $\lambda$  in Eqs. (1), (4) and (5) is the central wavelength value of the filter.

The image is resampled using bilinear interpolation if needed at each detector cell location to produce a pixelated version of the image on the CCD. The spectral irradiance at each detector cell,  $g_{ij}$  is converted to photon counts, and signal dependent Poisson noise is added at each pixel in the image. The detector cell model assumes a linear response with a saturation level set by the full well capacity of each detector cell. The number of electrons  $e^-$  at the  $i,j$ -detector cell is computed as

$$N_{ij}^{e^-} = \min[t_{exp}[g_{ij}QE + N_{ij}^{dc}], W_c] \quad (11)$$

where  $t_{exp}$  is the exposure time,  $g_{ij}$  is the number of photons recorded in the exposure time, QE is the average quantum efficiency over the observed spectral bandwidth,  $N_{ij}^{dc}$  is the number of electrons from one second of dark current (e-/sec), and  $W_c$  is the full well capacity of the detector cell. The photon electron counts are converted to counts using the quantization level of the CCD detector. When applied to the radiance maps produced by GHOST, the process for modeling realistic blurring and detection noise allows one to study different imaging scenarios in support of STM.

#### 4. MODELING GROUND-BASED IMAGERS

A variety of ground-based sensors support object identification and characterization tasks related to STM and SDA. Sensors such as wide FOV all-sky imagers provide synoptic information on RSOs and detect new unknown objects or debris. Sensors with a narrower FOV and higher resolution support characterization of RSOs based on photometric change detection and spatially resolved imagery. We demonstrate the use of DMISE-GHOST to address the development and optimization of both wide and narrow FOV imagers.

OMNISSA represents an all-sky imager based on the same philosophy as the Raven class telescopes, building a low-cost imager based on commercial off the shelf (COTS) components [1]. Accompanying an OMNISSA instrument would be the development of new robust streak detection and object classification algorithms. These algorithms would enable the extraction of information from large volumes of data collected by these all-sky imagers. Due to their lower cost, the placement of OMNISSA sensors at numerous geographically distributed locations could potentially provide synoptic observations of large volumes of near-Earth space. In such a scenario, it is essential to understand how sky-background noise and site-dependent atmospheric conditions affect the quality of the imagery and the subsequent ability to extract meaningful information for SDA tasks.

Using our M&S, we created imagery produced by the OMNISSA all-sky imager in an urban environment operating at visible wavelengths. The first step in computing a wide FOV image requires identifying all objects visible to the sensor. This task requires reading the Space catalog (from SpaceTrack.org) and using the (Two Line Element) TLE data with the SGP4 propagator to compute the location of each object and then determine if the space object is in the FOV of the sensor and illuminated by the Sun. When available, our simulation leverages CAD (computer-aided drafting) and MTL (material definitions file). For objects (out of a total of 17,356 processed from the catalog) that meet these conditions, their distance from the sensor is plotted as a function elapsed time in Fig 5. These results are filtered by DMISE and images for each sensors are rendered to include only objects visible. Based on the brightness of objects all-sky-imagers are most sensitive to orbits in LEO.

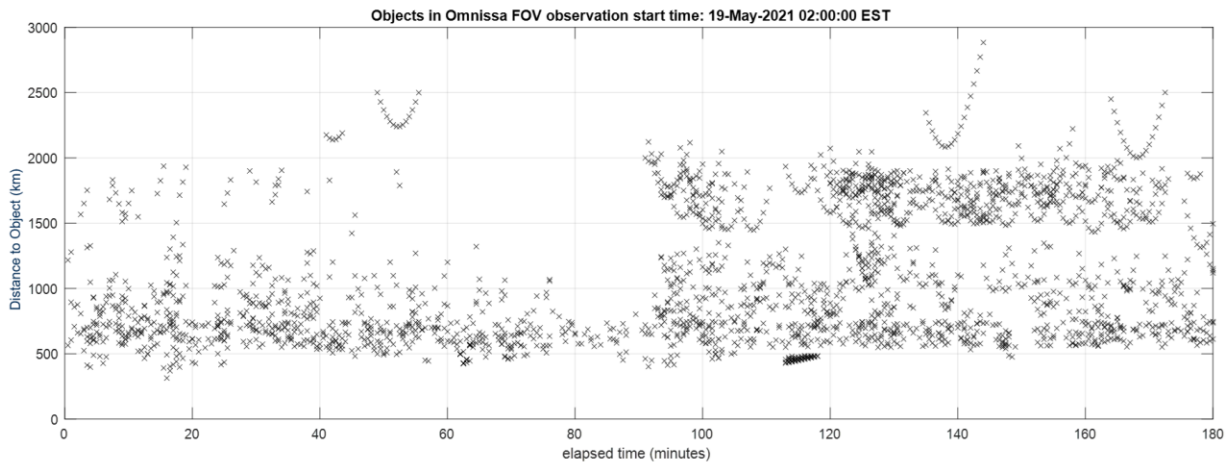


Fig 5: Plotted are the object distances as a function of time after identifying objects passing through the FOV of the sensors and illuminated by the Sun.

Fig 6 shows an example of a radiance map produced by GHOST of an OMNISSA imager with no optical aberrations, no sky background and no detector noise. The streak represents a relatively bright object ( $m_v = 4$ ), the signature of the Cosmos-2519 satellite as captured in a 20 second exposure. The parameters for this simulated image are shown in

Table 2: This scene includes the placement of the object’s streak with respect to the background stars in the image. Synthetic imagery of this type allows one to assess the performance of algorithms that identify streaks based on background stars.

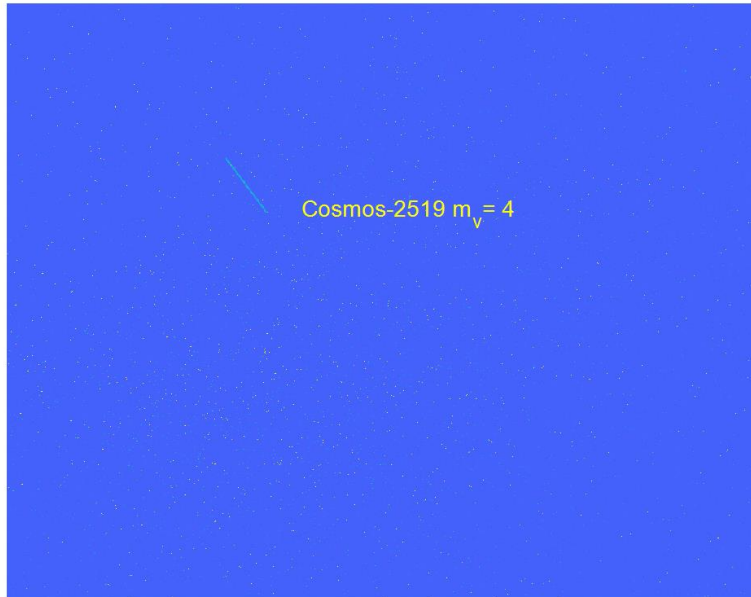


Fig 6: Radiance map of produced by GHOST with an exposure time of 20 seconds.

Table 2: Input parameters for simulation of radiance map produced by an OMNISSA all-sky-imager at visible wavelengths.

Parameter	Value
<b>FOV</b>	90 degrees
<b>Aperture</b>	0.0375 (m)
<b>Observation wavelength</b>	0.55 microns
<b>Spectral bandwidth</b>	0.128 microns
<b>Location</b>	Atlanta, GA
<b>Exposure Time</b>	20 seconds
<b>Number of pixels</b>	3326 x 2504
<b>Pixel Size</b>	5.4 microns

Optimizing an OMNISSA imager for certain geographic observing locations requires analyzing how specific filters allow one to extract the maximum information on space objects for a given level of sky background and light pollution. The GHOST capabilities complement current work at GTRI on optimizing filter selection for streak detection and identification in OMNISSA imagery in the presence of high sky background and light pollution [18]. Shown in Fig. 6 are simulated imagery of a streak in an OMNISSA image as observed through three different spectral filters.

We model the sky background noise and light pollution in these images consistent with the metropolitan Atlanta area observations. We compute the ratio of the streak counts to the background counts to yield a streak contrast ratio. In the presence of background noise and light pollution, the observation in the B-band yields the highest contrast ratio of 2.03. Conversely, the lowest contrast ratio of 1.12 occurs in the G-band image. The G-filter has larger spectral bandwidth, and thus, it collects more photons. However, more significant contributions from light pollution in this spectral band negates any gains in increased photons [19, 20]. These results are consistent with an analysis of observations [19] in Atlanta and obtained imagery from the OMNISSA camera at GTRI.

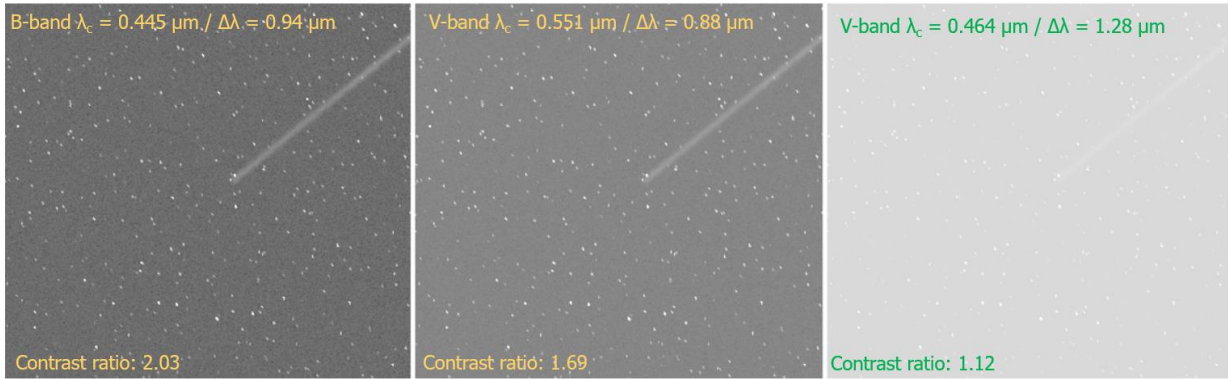


Fig 7: Image simulated by GHOST showing a streak in OMINSSA imagery with sky background and light pollution consistent with observations from metropolitan Atlanta area.

When detailed CAD and MTL files are available for a specific object, GHOST incorporates this information using the Sandford-Robertson BRDF model [21] when computing the radiance map for an object. Thus, we render a satellite's realistic radiance map, which includes its geometry, surface materials, and the actual illumination and viewing geometry occurring during the observation. Shown in Fig 8 are examples of spatially resolved imagery produced by GHOST. From left to right are the radiance map, a short exposure image (the exposure time is comparable to the coherence time of the atmosphere, effects of Poisson, and read out noise which is evident), and a long exposure image (the exposure time is much greater than the coherence time).

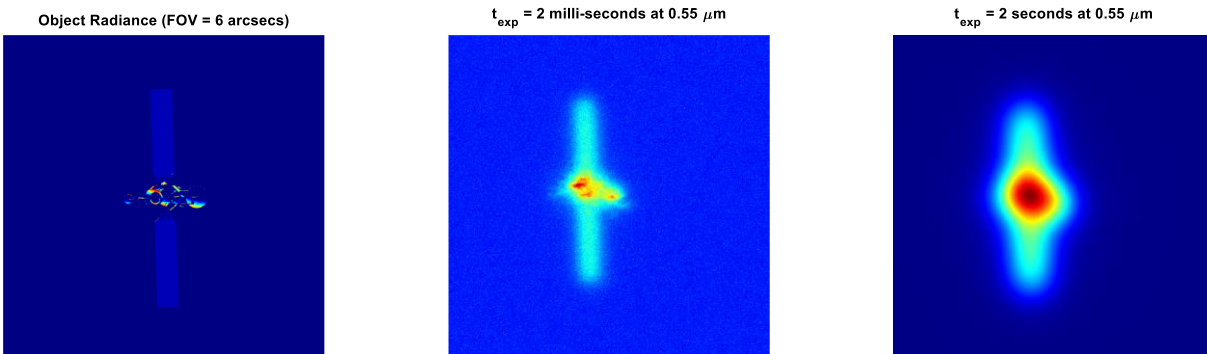


Fig 8 Left: Radiance map of satellite, Center: Short exposure image for a 3-m class telescope, Right: Long exposure image

The ability to render realistic ground-based imagery allows one to generate large datasets for particular engagement scenarios that might possibly occur in the future. The capability of machine learning and model algorithms to extract information relative to STM tasks can thus be evaluated on these datasets where the truth is known.

## 5. SPACE-BASED IMAGERS

Building and implementing a robust space traffic system will require new ground- and space-based sensors that routinely collect information on the presence and distribution of debris and other space objects in the known satellite orbital belts. While RADAR offers the capability to detect space debris and other space objects down to 2cm in size [22], it provides little information on the object's material properties besides RADAR cross-section (RCS). This type of information would enable object classification and further characterization. Obtaining this information on materials requires studying the reflected solar radiation from an object at different wavelengths, from the ultra-violet to the far-infrared, and extracting the object's spectral fingerprint [23].

We examine a scenario where a proposed imager, supporting STM efforts, surveys the orbital regimes occupied by mega satellite constellations and identifies any possible debris that may pose a collision threat to members of the constellation. Discriminating between an actual Starlink satellite and debris requires *a priori* information about Starlink satellites, such as knowledge of the surface materials on the satellite. With this prior knowledge, measuring

the reflected solar illumination at different wavelengths from a satellite allows one to obtain a spectral signature. This signature can be compared to laboratory measurements for the known materials on the satellite. By comparing these two signatures, one may gather evidence to support an assertion of whether the unidentified object is a member of the satellite constellation.

A spectral signature requires observations at multiple wavelengths the value of the material's reflectivity depends on the wavelength of incident light. Due to the limited atmospheric transmission at specific wavelengths, a space-based imager offers advantages over ground-based imaging, especially in the ultra-violet and infrared parts of the spectrum. Typical materials on spacecraft exhibit reflectivity values that change as a function of observing wavelength, especially in the infrared..

Fig 9 shows an example of the reflectivity values for three common materials used on satellites. These materials exhibit very different signatures from 0.350 microns to 2.4 microns [24]. The approach to obtaining spectral signatures studied involves determining a set of spectral filters that allows one to discriminate between material types based on the material reflectivity values in different spectral bands. We collect imagery at various wavelengths under nearly identical illumination conditions, which requires high cadence (short exposure time) imagery. In contrast to a hyperspectral imager which gives higher spectral resolution, our approach yields a low spectral resolution signature producing data with a higher SNR due to the spectral integration over the filter bandwidth.

We modeled the reflected light from a Starlink satellite coming from *Silicon solar cells* and light from the unknown target coming from *Germanium solar cells*. We chose these materials to test a binary classification algorithm that classifies an object as a member of the Starlink constellation. By limiting our satellite model to only a single material, we approximate the case where this single material represents the dominant or majority material covering the target. Thus the reflected light comes from a single spacecraft material on the satellite and not a mixture of materials. Our single material assumption results in approximate modeling of the problem, assuming the reflected light from non-dominant materials is small compared to the light reflected from the primary material. In scenarios where this assumption does not apply, it will be necessary to perform spectral unmixing; a level of complexity not considered here.



Fig 9: Reflectance for Solar Cell Materials (Germanium and Silicon) and Mylar – Discriminator filters placed at chosen observation wavelengths.

Based on the laboratory measured reflectivity values in Fig 9, the spectral signatures for *Silicon* and *Germanium* solar cell materials are computed via the flux ratios measured at two wavelengths.

We considered the HAWAII-4RG [25] as a potential camera for the imager. The HAWAII-4RG has high quantum efficiency over both visible and infrared wavelengths and a large format, 4096 x 4096 pixels, a pixel size of, and a read noise of 10 e-. The optical system for the imager has a FOV of 1° x 1°, F/# = 8.4, and an aperture diameter of 0.15 meters. This FOV gives as broad a search area as possible for a single image, thus capturing both targets in the same scene. This FOV, therefore, minimizes the need for maneuvering and pointing the sensor. Further, this optical configuration allows us to maintain sufficient sampling of the PSF by the focal plane array (FPA).

We model the imager trailing Starlink-1014 in its orbital trajectory with the distance between the imager and Starlink-1014 equal to 2400 km. Following the Starlink satellite in this orbit is an unidentified space object. The distance between Starlink-1014 and the unidentified object is 34.2 km. This viewing geometry combined with the FOV of our imager allows us to image both targets in the same scene. Further, we model the observation occurring when both targets are greater than 25 degrees away from Earth's limb (resulting from the Earth's atmosphere). In this scenario, the background contributions in V magnitude per arcsec<sup>2</sup> equals 21 due to the zodiacal light, Moon, and sunlit Earth [26]. Using DMISE-GHOST and the sensor modules, we modeled the engagement scenario producing two sequences of images at  $\lambda = 0.950 \mu\text{m}$  and  $1.4 \mu\text{m}$ . A single image from the  $0.95 \mu\text{m}$  sequence with an exposure time of  $t_{exp} = 500$  milliseconds is shown in Fig 10. Again, the motivation for this high cadence imaging was to measure the reflected solar illumination from both objects under nearly identical illumination conditions at two different wavelengths and thus extract spectral signatures for each target.

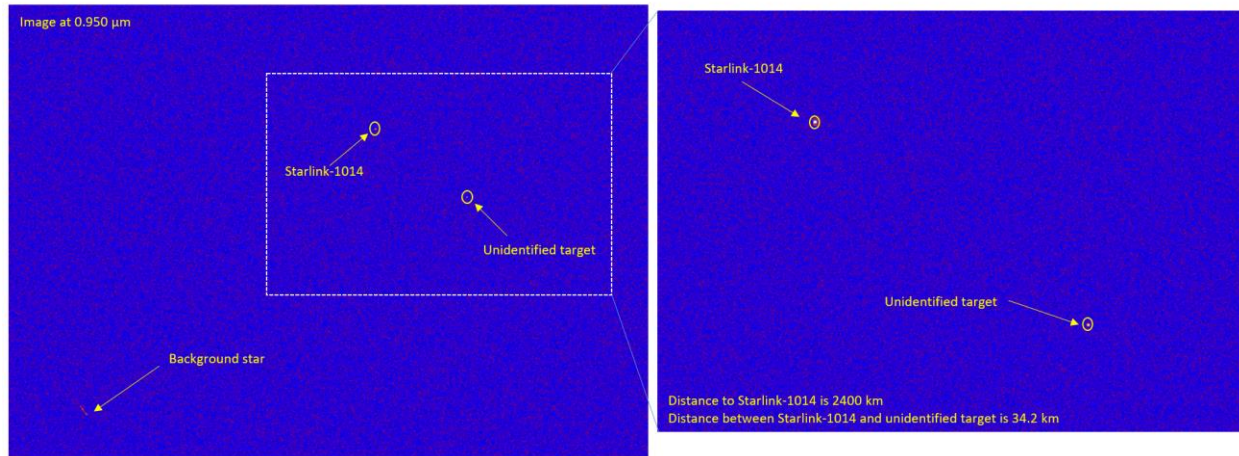


Fig 10: A rendered DMISE-GHOST image from the sequence of images at 0.95 microns showing Starlink-1014, an unidentified object, and background star. Images have realistic sensor modeling of the Hawaii-4RG CCD.

The spectral signatures are obtained by first identifying the targets in the image, computing the flux values over the pixels in an aperture circle centered over each target, and then computing the ratio of the fluxes between the SWIR (1.4-1.45  $\mu\text{m}$ ) and R (0.9-0.95  $\mu\text{m}$ ). In the measurements, offsets are applied to the target flux values to compensate for the varying amounts of solar irradiance at the different wavelengths. After this correction, any differences in flux ratios depend on the reflectance properties of the materials. The ratio of the observed flux for the Starlink-1014 satellite in the SWIR band to the R band is 13.66 +/- 1.16 compared to the laboratory measured reflectivity ratio equal to 15.2. The same ratio for the unidentified object is 0.93 +/- 0.075. These results are summarized in Table 3.

Table 3: Comparison of Observed vs Laboratory measured spectral signatures

Material Type	Measured Reflectivity $\lambda_c=0.95 \mu\text{m}$	Measured Reflectivity $\lambda_c=1.40 \mu\text{m}$	Laboratory $R_{\text{SWIR}}/R_{\text{R}}$	Observed signature $F_{\text{SWIR}}/F_{\text{R}}$ (noise)
Solar Cell	0.025	0.39	15.6	13.66 +/- 1.16
Germanium	0.025	0.025	1.0	0.9257 +/- 0.0757

After integrating the counts for each target in the image, the background noise contaminates the measured flux value for each target. The most likely source of error in the estimated signature values. Our requirement to collect

observations under the same illumination conditions motivated the short exposure time of 0.5 seconds. Relaxing the illumination requirement would allow us to increase the integration time, thus improving the SNR and the fidelity of the estimated spectral signature. The flexibility of DMISE-GHOST will enable one to vary specific design parameters, such as optics FOV, sensor characteristics, observation wavelengths, exposure times, and orbital regimes to study how each factor affects STM objectives for the mission.

## 6. CONCLUSIONS AND FUTURE WORK

The ability to simulate engagement scenarios in space with numerous actors while modeling realistic sensor observations of these interactions is a powerful tool for developing strategies for effective use of space resources. The DMISE-GHOST modeling and simulation environment allows one to begin studying the problem of identifying and characterizing the interaction of satellites and space debris in the near-Earth space environment. Realistic synthetic imagery of both ground- and space-based imagers allows one to begin addressing the problem of developing sensors and algorithms to support space traffic management. Future work will focus on the design of potential space-based imagers to support SDA efforts. Further, we plan to investigate how ground- and space-based sensors could collaboratively identify and characterize space objects and possible hazardous debris.

## 7. REFERENCES

- [1] M. E. Grøtte, S. Virani, M. J. Holzinger, A. Register, C. A. Perez, and J. E. Tapia, "All-Sky Image Fusion for a Synoptic Survey Telescope in Arctic and Antarctic Domains," Advanced Maui Optical and Space Surveillance Technologies Conference (2016).
- [2] Deborah F. Woods, Ronak Shah, Julie A. Johnson, Alexander Szabo, Eric C. Pearce, Richard L. Lambour, Walter J. Faccenda, "Space Surveillance Telescope: focus and alignment of a three mirror telescope," Opt. Eng. 52(5) 053604 (7 May 2013)
- [3] R. D. Coder. Multi-Objective Design of Small Telescopes and Their Application to Space Object Characterization. PhD thesis, Georgia Institute of Technology, Atlanta, GA, August 2015.
- [4] Paul F. Sydney, John L. Africano, Amy Fredericks, Kris M. Hamada, Vicki Soo Hoo, Daron L. Nishimoto, Paul W. Kervin, Steve Bisque, Matthew Bisque, "Raven automated small telescope systems," Proc. SPIE 4091, Imaging Technology and Telescopes, (31 October 2000); <https://doi.org/10.1117/12.405780>
- [5] Roberts, L.C. & Neyman C.R. 2002, Pub. Astro. Soc. Pacific, 114, 1260-1266, Characterization of the AEOS Adaptive Optics System
- [6] Robert Q. Fugate, "The Starfire Optical Range 3.5-m adaptive optical telescope," Proc. SPIE 4837, Large Ground-based Telescopes, (4 February 2003); <https://doi.org/10.1117/12.457972>
- [7] Vallado, D. and Crawford, P., *SGP4 Orbit Determination*, AIAA/AAS Astrodynamics Specialist Conference and Exhibit (2012)
- [8] Kelso, T. S. 2007. "Validation of SGP4 and IS-GPS-200D Against GPS Precision Ephemerides." Paper AAS 07-127 presented at the AAS/AIAA Spaceflight Mechanics Conference. Sedona, Arizona.
- [9] "Wavefront OBJ File Format," Jan. 23, 2020. <https://www.loc.gov/preservation/digital/formats/fdd/fdd000507.shtml> (accessed Jun. 04, 2021).
- [10] Nash, David, HYG Database, [Online]. Available: <http://www.astronexus.com/hyg>
- [11] Hoffleit, D. and Warren, Jr., W.H., 1991, "The Bright Star Catalog (1991). [Online]. Available: <https://heasarc.gsfc.nasa.gov/W3Browse/star-catalog/bsc5p.html>
- [12] Astronomical Almanac for the Year 2015, United States Government Printing Office (2014)
- [13] Keith F. Prussing, Christopher R. Valenta, Christopher E. Cordell, Anissa Zacharias, Layne R. Churchill, "Stellar background rendering for space situational awareness algorithm development," Proc. SPIE 10986, Algorithms, Technologies, and Applications for Multispectral and Hyperspectral Imagery XXV, 109860Z (14 May 2019); <https://doi.org/10.1117/12.2519009>
- [14] Goodman, Joseph, *Statistical Optics*, Wiley-Interscience, 1985
- [15] Claire Max, Center for Adaptive Optics, UC-Santa Cruz, Lecture 5: Imaging through Turbulence
- [16] Fried, D. L. (October 1966). "Optical Resolution Through a Randomly Inhomogeneous Medium for Very Long and Very Short Exposures". Journal of the Optical Society of America. 56 (10): 1372–1379.
- [17] Cressida M. Harding, Rachel A. Johnston, and Richard G. Lane, "Fast simulation of a kolmogorov phase screen," Appl. Opt. 38, 2161-2170 (1999)
- [18] Boreman, G.D., *Modulation Transfer Function in Optical and Electro-Optical Systems*, 2<sup>nd</sup> Ed., SPIE Press (2021)

- [19] Badura, G., Valenta, C.R., Gunter, B., Renegar, L., and Wu, Devin, *Spectral Performance Optimization of Small Telescopes For Space Object Detection*, in Advanced Maui Optical and Space Surveillance Technologies Conference (2019)
- [20] Coder, R. and M. J. Holzinger, "Sizing of a Raven-class telescope using performance sensitivities," Advanced Maui Optical and Space Surveillance Technologies Conference (2013).
- [21] . B. P. Sandford and D. C. Robertson, Infrared reflectance properties of aircraft paints, U. S. Air Force Research Laboratory Preprint AFRL/VSBT ESC-94-1004, approved for public release August 1994.
- [22] Erwin, Sandra, "Space Fence surveillance radar site declared operational," *Space News* (March 2020)
- [23] Reyes, Jacqueline A. and Cone, Darren, "Characterization of spacecraft materials using reflectance spectroscopy," Advanced Maui Optical and Space Surveillance Technologies Conference (2018).
- [24] NASA JSC Spacecraft Materials Spectral Database
- [25] Markus Loose, James Beletic, James Garnett, Min Xu, "High-performance focal plane arrays based on the HAWAII-2RG/4RG and the SIDECAR ASIC," Proc. SPIE 6690, Focal Plane Arrays for Space Telescopes III, 66900C (17 September 2007); <https://doi.org/10.1117/12.735625>
- [26] Hubble Space Telescope - *Wide Field Camera 3 Instrument Handbook*, Space Science Telescope Institute.

## 8. ACKNOWLEDGEMENTS

This work was supported by Internal Research and Development funding from the Georgia Tech Research Institute. The material reflectance curves are from the NASA JSC spectral materials database. Dr. Jackie Reyes (Univ. of Texas – El Paso) helped prepare the material reflectance plots.